Spectrum and Polarization of the Galactic Center Radio Transient ASKAP J173608.2–321635 from THOR-GC and VLITE

Kierra J. Weatherhead[1] , Jeroen M. Stil[1] , Michael Rugel[2,3] , Wendy M. Peters[4] , Loren Anderson[5,6,7] , Ashley Barnes[8] ,
Henrik Beuther[9] , Tracy E. Clarke[4] , Sergio A. Dzib[10] , Paul Goldsmith[11] , Karl M. Menten[10] , Kristina E. Nyland[4] ,
Mattia C. Sormani[12] , and James Urquhart[13]

[1] Department of Physics and Astronomy, The University of Calgary, 2500 University Drive NW, Calgary AB T2N 1N4, Canada
[2] Center for Astrophysics, Harvard & Smithsonian, 60 Garden St., Cambridge, MA 02138, USA
[3] National Radio Astronomy Observatory, 1003 Lopezville Rd, Socorro, NM 87801, USA
[4] U.S. Naval Research Laboratory, 4555 Overlook Ave. SW, Washington, DC 20375, USA
[5] Department of Physics and Astronomy, West Virginia University, Morgantown, WV 26506, USA
[6] Adjunct Astronomer at the Green Bank Observatory, P.O. Box 2, Green Bank, WV 24944, USA
[7] Center for Gravitational Waves and Cosmology, West Virginia University, Chestnut Ridge Research Building, Morgantown, WV 26505, USA
[8] European Southern Observatory (ESO), Karl-Schwarzschild-Straße 2, 85748 Garching, Germany
[9] Max Planck Institute for Astronomy, Königstuhl 17, D-69117 Heidelberg, Germany
[10] Max-Planck-Institut für Radioastronomie, Auf dem Hügel 69, D-53121 Bonn, Germany
[11] Jet Propulsion Laboratory, California Institute of Technology, 4800 Oak Grove Dr., Pasadena, CA 91109, USA
[12] Università dell'Insubria, via Valleggio 11, 22100 Como, Italy
[13] Centre for Astrophysics and Planetary Science, University of Kent, Canterbury CT2 7NH, UK

Abstract

The radio transient ASKAP J173608.2–321635, at the position $(\ell, b) = (356°.0872, -0°.0390)$, was serendipitously observed by The H I/OH/Recombination line survey of the Galactic center at three epochs in 2020 March, 2020 April, and 2021 February. The source was detected only on 2020 April 11 with a flux density of 20.6 ± 1.1 mJy at 1.23 GHz and in-band spectral index of $\alpha = -3.1 \pm 0.2$. The commensal Very Large Array Low-band Ionosphere and Transient Experiment simultaneously detected the source at 339 MHz with a flux density of 122.6 ± 20.4 mJy, indicating a spectral break below 1 GHz. The rotation measure (RM) in 2020 April was 63.9 ± 0.3 rad m^{-2}, which almost triples the range of the variable RM observed by Wang et al. to ~130 rad m^{-2}. The polarization angle, corrected for Faraday rotation, was $97° \pm 6°$. The 1.23 GHz linear polarization was $76.7\% \pm 3.9\%$ with wavelength-dependent depolarization, indicating a Faraday depth dispersion of $\sigma_\phi = 4.8^{+0.5}_{-0.7}$ rad m^{-2}. We find an upper limit to the circular polarization of $|V|/I < 10.1\%$. Interpretation of the data in terms of diffractive scattering of radio waves by a plasma near the source indicates an electron density and a line-of-sight magnetic field strength within a factor of 3 of $n_e \sim 2$ cm^{-3} and $B_\parallel \sim 2 \times 10^5$ μG. Combined with causality limits to the size of the source, these parameters are consistent with the low-frequency spectral break resulting from synchrotron self-absorption, not free–free absorption. A possible interpretation of the source is a highly supersonic neutron star interacting with a changing environment.

Unified Astronomy Thesaurus concepts: Interstellar magnetic fields (845); Radio transient sources (2008); Sky surveys (1464); Radio bursts (1339); Galactic radio sources (571)

1. Introduction

Increases in survey speed, wide-field capability, and capabilities for commensal surveys have increased the chance of detection of transient radio continuum sources with a variety of origins such as fast radio bursts (FRBs; Petroff et al. 2022), rotating radio transients (McLaughlin et al. 2006), radio afterglows of gamma-ray bursts (Frail et al. 1997), tidal disruption events (Anderson et al. 2020), stellar flares (Roy et al. 2010), and intermittent pulsars (Kramer et al. 2006). Establishing basic observational parameters is important to uncover the underlying physical phenomena, but it can be challenging when sources change in an unpredictable way on short timescales. Some radio interferometers are capable of simultaneous wide-field, high-time resolution, and high-angular resolution observations. Examples are the Australian Square

Kilometre Array Pathfinder (ASKAP; Hotan et al. 2021), the South African Square Kilometre Array precursor MeerKAT (Jonas & MeerKAT Team 2016), the Low-Frequency Array (van Haarlem et al. 2013), the Murchison Wide-field Array (Tingay et al. 2013), the Allen Telescope Array (ATA; Croft et al. 2010), and the Canadian H I Intensity Mapping Experiment (CHIME; CHIME Collaboration et al. 2022) with its outrigger stations. Sometimes, surveys that are not designed to observe transients make significant serendipitous observations of transient sources, as in the case of this paper.

The unresolved, erratic radio transient ASKAP J 173608.2–321635 was first discovered in 2020 January when data from the Variables and Slow Transients Phase 1 Pilot Survey (Murphy et al. 2013) were searched for transient sources. This source had not been detected in ASKAP observations prior to this, between 2019 April and 2019 October. ASKAP measurements between 2020 January and 2020 August found J173608.2–321635 to be variable and also highly circularly polarized. Later measurements by MeerKAT in 2021 February also found the source to be highly linearly polarized. The

Table 1
THOR and VLITE Flux Density and Polarization Measurements

Civil Date	Epoch (MJD)	ν (MHz)	S_ν (mJy)	α	Π_ν (%)	θ (deg)	RM (rad m^{-2})	σ_ϕ (rad m^{-2})	V_ν/I_ν (%)
2020 March 17	58925[a]	339	<34.5	...	...	...	...	...	...
		1243[c,d]	<6.8	...	...	...	...	...	...
2020 April 11	58950[a]	339	122.6 ± 20.4	−1.0 ± 0.2[f]	...	...	...	...	...
		1233[c,d]	20.6 ± 1.1	–3.1 ± 0.2	76.7 ± 3.9	–46.7 ± 0.3	63.9 ± 0.3	$4.8^{+0.5}_{-0.7}$	<10.1[g]
2021 April 28	59332[b]	1435[c,e]	<11.4	...	...	...	...	...	...

Notes.
[a] C-configuration.
[b] D-configuration.
[c] Frequencies from 2020 March 17 and 2021 April 28 are derived from multifrequency synthesis and frequency from 2020 April 11 is derived from RM synthesis.
[d] Includes measurements from subbands centered at 1.051 and 1.435 GHz.
[e] Includes measurements from subbands centered at 1.435 GHz.
[f] Spectral index between 339 MHz and 1 GHz.
[g] Upper limit for circular polarization at 1.248 GHz.

nature of ASKAP J173608.2–321635 is unclear. ASKAP J 173608.2–321635 has similar parameters to other transient sources near the Galactic center, including its steep spectral index that varies from $\alpha = -2.7$ to -5.6, where $S_\nu \sim \nu^\alpha$ (Wang et al. 2021). Some Galactic center radio transients (GCRTs) have also been reported with very steep spectral indices. GCRT J1742–3001 was found to have a spectral index of $\lesssim -2$ between 235 and 610 MHz by Hyman et al. (2009). GCRT J1745–3009 has a variable in-band spectral index at 325 MHz ranging from -4 to -13.5 (Hyman et al. 2007; Roy et al. 2010).

Wang et al. (2021) and Wang et al. (2022) found ASKAP J173608.2–321635 to have a high degree of linear polarization, nearly 100% at 1.6 GHz, and variable circular polarization up to $\sim 40\%$ at 0.9 GHz in two separate observations in 2020 and 2021. Roy et al. (2010) reported variable circular polarization up to 100% for the GCRT J1745–3009.

The outburst of ASKAP J173608.2–321635 that led to its discovery by ASKAP was serendipitously observed with the Karl G. Jansky Very Large Array (VLA) during observations for the extension toward the Galactic center of The H I/OH/ Recombination line survey of the inner Milky Way (THOR; Beuther et al. 2016).

The THOR Galactic Center extension (THOR-GC) covers $-6° < l < 15°$ with $|b| < 1°.25$. Fortuitously, the VLA Low-Band Ionosphere and Transient Experiment (VLITE; Clarke et al. 2016)[14] system was operational at the time, providing us with simultaneous low-frequency data at 339 MHz. In this work, we present the new observations of ASKAP J173608.2–321635 from the THOR-GC survey and discuss some possible interpretation in view of the new results.

2. Observations and Data Reduction

2.1. THOR-GC

The H I/OH/Recombination line Survey of the inner Milky Way (THOR; Beuther et al. 2016) is an L-band (1–2 GHz) survey with the Jansky VLA of the interstellar medium (ISM) in the inner Galaxy, with separate data products for spectral

lines of the H I 21 cm line, four 18 cm OH lines, several hydrogen recombination lines, and the continuum. Details of the observational setup, calibration, and imaging were described by Beuther et al. (2016) and in particular for the continuum polarization by Shanahan et al. (2022). THOR-GC (VLA project 20A-160) is an extension of the THOR survey toward and across the Galactic center region, with the same data products. A notable difference between THOR and THOR-GC is that THOR was observed in C-configuration only, using D-configuration data from the VLA Galactic Plane Survey (Stil et al. 2006, H I line and 1.4 GHz continuum only) that were observed before the upgrade of the VLA. THOR-GC observed ASKAP J173608.2–321635 in C-configuration on 2020 March 17 and 2020 April 11 and with a short snapshot in D-configuration on 2021 April 28.

Calibration and imaging were performed in the CASA environment 6.5.0 (CASA Team et al. 2022) following standard procedures. THOR-GC includes six of the continuum subbands used in THOR. In this work, we present observations from subbands centered at 1.05 and 1.44 GHz, each with a bandwidth of 128 MHz. The spectrum of the source was so steep that it was not detected in our higher frequency subbands.

The Stokes I visibility data were averaged to 20 MHz channels, while the Stokes Q and U visibility data were averaged to 4 MHz channels before imaging to improve the signal-to-noise ratio per channel for cleaning. The averaging reduces the maximum observable Faraday rotation to 2.4×10^3 rad m^{-2} at 1 GHz, which is sufficient for the purpose of this paper. The Stokes V visibility data were averaged over the two subbands in which ASKAP J173608.2–321635 was visible in Stokes I. The Q, U, and V images were convolved to a common angular resolution of $45'' \times 20''$ using the CASA task imsmooth, with pixels of size $2.''5 \times 2.''5$. For each polarization image, a Stokes I image with the same angular resolution was made.

For the analysis of ASKAP J173608.2–321635, the observations of the three epochs were imaged separately as outlined in Table 1. The final images used in the analysis were made using the surrounding 25 pointings. Each pointing in the mosaic was imaged to a radius where the sensitivity dropped to 20%. As such, 6–11 of the 25 imaged pointings, depending on frequency, covered the location of ASKAP J173608.2–321635. The source

---

[14] https://vlite.nrao.edu

was near the center of one pointing, at a distance of $3'\!.25$, and the center of the furthest pointing, which covered the source at all frequencies used in the analysis, was at a distance of $17'\!.96$. The six pointings were each observed on three scans of the sky over a span of 3.59 hr. The average integration time of each scan for the six pointings was 1.72 minutes, and each pointing had an average total integration time of 5.17 minutes. We tried to image individual fields to investigate variability on timescales of minutes, but this proved inconclusive because the integration time of the individual snapshots was short, and the steep spectrum of the source significantly reduced the effective bandwidth.

Stokes Q and U spectra were extracted by summation over a box of size 4×4 pixels centered on ASKAP J173608.2–321635. These Q and U spectra were subsequently analyzed with methods designed for broad-band radio polarimetry called Faraday rotation measure (RM) synthesis (Brentjens & de Bruyn 2005) and QU fitting (Law et al. 2011; O'Sullivan et al. 2012). For a linearly polarized wave with wavelength λ, traveling through a magnetized plasma with electron density n_e and magnetic field with line-of-sight component $B_{\parallel}$, the polarization angle θ changes by an amount $\phi\lambda^2$ with the Faraday depth ϕ defined as

$$\phi = \frac{e^3}{2\pi m_e^2 c^4} \int n_e B_{\parallel} \mathrm{d}l, \tag{1}$$

with e the elementary charge, m_e the mass of an electron, and c the speed of light. The integral is performed from the source to the observer, with positive ϕ indicating a mean magnetic field directed toward the observer.

If we encounter a situation in which waves experiencing different amounts of Faraday rotation are blended, the superposition of the polarization states of these waves leads to changes in the observed fractional polarization with wavelength and also deviations from the λ^2 dependence of the polarization angle that can be observed in polarimetry data with good spectral resolution over a wide wavelength range.

In RM synthesis[15] (Brentjens & de Bruyn 2005), the Stokes Q and U spectra are divided by the Stokes I spectrum and combined into the complex polarization $\mathcal{P} = q + iu$, with $q = Q/I$ and $u = U/I$. The division by Stokes I eliminates the power-law spectral dependence of optically thin synchrotron emission, which has constant fractional polarization. Introducing a weight function $W(\lambda^2)$ that is zero for any wavelength λ for which no measurements are available, the Fourier transform of $P(\lambda^2)W(\lambda^2)$ is the observed Faraday dispersion function (FDF) $\tilde{\mathcal{F}}$,

$$\tilde{\mathcal{F}} = \frac{\int W(\xi)\mathcal{P}(\xi)e^{-2i\phi\xi}d\xi}{\int W(\xi)d\xi}, \tag{2}$$

where $\xi = \lambda^2$ if $\xi > 0$. As no measurements can be made for $\xi \leqslant 0$, $W(\xi) = 0$ for these values to extend the bounds of the Fourier transform over the required range (Brentjens & de Bruyn 2005). In this work, we apply uniform weights for all wavelengths where measurements were made.

In principle, the FDF is the distribution of polarized intensity as a function of Faraday depth. In practice, $\tilde{F}$ is the convolution of the true FDF with the Fourier transform of $W(\xi)$ and a deconvolution is necessary (Heald 2009).

---

[15] This work uses `RM-Tools` (Purcell et al. 2020) for the analysis of polarization data.

QU fitting achieves the same goals as RM synthesis in λ^2 space by fitting a model to the complex polarization. A useful model for analysis of the current data is (e.g., Burn 1966; O'Sullivan et al. 2012; Feng et al. 2022)

$$\mathcal{P} = P_0 e^{-2\sigma_\phi^2 \lambda^4} e^{2i(\theta_0 + \phi_0 \lambda^2)}. \tag{3}$$

In this function, the fitting parameters are P_0, the (real-valued) fractional polarization in the absence of any Faraday rotation, σ_ϕ, the Faraday depth dispersion, and ϕ_0, the mean Faraday depth, also referred to as the RM. This model is useful when fitting modest depolarization over the observed frequency range, yielding a mean and standard deviation of the FDF. It has been shown to fit the depolarization of FRBs well (Feng et al. 2022), although its physical interpretation of a turbulent foreground screen with many unresolved independent cells covering a source (Burn 1966) does not align well with the compact nature of these sources.

The standard THOR-GC data products combine the results of both C- and D-configuration observations. In this paper, we investigate a continuum transient source that requires imaging of the individual observing epochs. After some experimentation, it was decided that removing baselines shorter than 500 m (14% of the visibilities) did not significantly improve the quality of the images, and data obtained with all baselines could be used in the imaging of the L-band data. We note that ASKAP J173608.2–321635 is too faint to detect any absorption in the H I 21 cm line data.

2.2. VLITE Data Processing

Data from VLITE were recorded simultaneously using 18 antennae during the THOR-GC observations described above in the VLA's C-configuration on 2020 March 17 and 2020 April 11. The VLITE 2021 D-configuration data did not have sufficient angular resolution to reliably separate the transient source from surrounding structures, and those data are not included here. All VLITE data are processed within a few days of observation by a dedicated calibration and imaging pipeline, which combines Python with standard processing tasks found in AIPS (Greisen 2003) and Obit (Cotton 2008). Full details of the VLITE calibration pipeline are described in Polisensky et al. (2016). For both of the 2020 observing sessions, 3C286 was used for primary calibration, and an NVSS image (Condon et al. 1998) was used as a sky model to correct for ionospheric phase contribution in the target direction. The data have a final bandwidth of 34 MHz centered at 339 MHz on both days, and an angular resolution of $86'' \times 22''$ at $0°\!.63$ and $60'' \times 26''$ at $16.°9$ on March 17 and April 11, respectively.

In order to match the higher frequency analysis, we used the same 25 surrounding THOR-GC pointings within a radius of $0°\!.72$ of the target, observed over a span of 3.95 hr. The uv-data for each of these were shifted to a common reference center at the position of the source of interest using the AIPS task `UVFIX`, and then combined for each of the two dates. The combined data were manually flagged to remove any remaining radio frequency interference, and then imaged using the Obit task `MFImage`, with a single phase-only self-calibration loop, using a 6 s solution step, to ensure all the data were well-aligned. In order to minimize the contribution of large-scale Galactic structures, during the imaging step we removed the shortest baselines ($< 0.4\,\mathrm{k}\lambda$), and used a slightly uniform weighting scheme (robust factor of -1.5). The images were
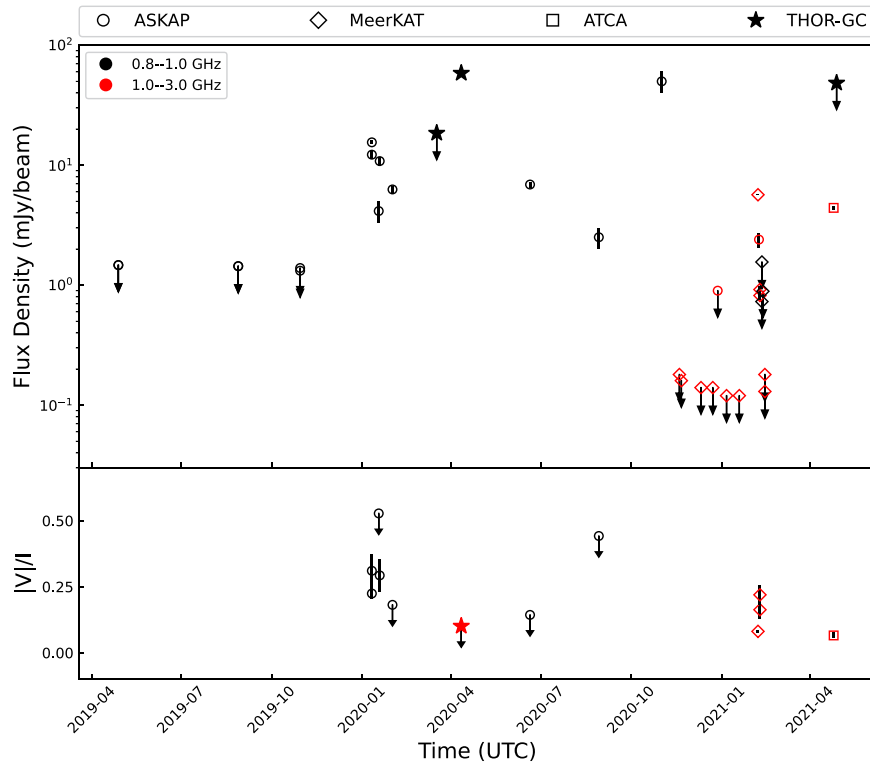
Figure 1. Flux density of ASKAP J173608.2–321635 as a function of time (adapted from Wang et al. 2021). The ASKAP, MeerKAT, and ATCA flux densities are from Wang et al. (2021). The color of the symbols indicates the same broad frequency ranges as in Wang et al. (2021). Arrows indicate 3σ upper limits. THOR-GC total flux densities and upper limits have been extrapolated to 900 MHz, assuming a spectral index of $\alpha = -3.1$. The THOR-GC circular polarization upper limits are for $\nu = 1.23$ GHz (Table 1). The bottom panel shows the fractional circular polarization of the source.

corrected using VLITE-specific beam models that were averaged to properly account for the original telescope positions.

The final images have rms noise levels at the position of the source of $\sigma = 11.5$, and 10.2 mJy beam^{-1} on March 17 and April 11, respectively. The source is not seen on the first day, but is detected at a signal-to-noise ratio of 12 with a flux of 122.6 ± 20.4 mJy on April 11.

3. Results

3.1. Variability

ASKAP J173608.2–321635 was not detected in two epochs of THOR-GC on 2020 March 17 and 2021 April 28. Averaging over a single spectral window, 3σ upper limits of 13.5 and 4.3 mJy were found for the epoch on 2020 March 17 at 1.051 and 1.435 GHz, respectively, and 11.4 mJy for the epoch on 2021 April 28 at 1.435 GHz. Averaging over two spectral windows for the 2020 March 17 observation, a 3σ upper limit of 6.8 mJy was found at 1.243 GHz. The source was strongly detected in our observation on 2020 April 11 with a flux density of 20.6 ± 1.1 mJy at a centroid frequency of 1.233 GHz. Figure 1 shows the flux density of the ASKAP J173608.2–321635 detection and upper limits in THOR-GC with measurements made by Wang et al. (2021).

Based on this detection, the best-fit position of the source is R.A. (J2000) $17^h36^m8{.}^s25 \pm 0{.}^s09$, decl. (J2000) $-32°16'31{.}''71 \pm 1{.}''9$, with Galactic coordinates $(l, b) = (356{.}°0872°, -0{.}°0390)$. The best-fit position from the VLITE measurement on the same day is R.A. (J2000) $17^h36^m8{.}^s21 \pm 0{.}^s15$, decl. (J2000) $-32°16'41{.}''18 \pm 8{.}''56$, $(l, b) = (356{.}°0849, -0{.}°0403)$. Figure 2 shows the surroundings of ASKAP J173608.2–321635 in

THOR-GC and VLITE. Flux densities and other source parameters are listed in Table 1.

3.2. X-Ray Observations

The extended ROentgen Survey with an Imaging Telescope Array (eROSITA; Predehl et al. 2021) all-sky survey includes X-ray observations at soft (0.2–0.6 keV), medium (0.6–2.3 keV), and hard (2.3–5.0 keV) energy bands. The hard energy band is the least susceptible to absorption, and so we use this band in our analysis. eROSITA (data release 1, 2024 January 31) observed this region of the sky in the hard energy band between 2020 March 24 and 2020 March 28 for 77 s. There were no counts within $4''$ of ASKAP J173608.2–321635. This yields an upper limit on the flux of 1.00×10^{-12} erg s^{-1} cm^{-2} from 2.3–5.0 keV (Merloni et al. 2024; Tubín-Arenas et al. 2024). This corresponds to an upper limit of $1.20 \times 10^{34}(d/10 \,\mathrm{kpc})^2$ erg s^{-1} for the X-ray luminosity at a distance d. This upper limit excludes a powerful burst of a magnetar near the Galactic center (see the discussion in Wang et al. 2021) at the time of the observation, but the sensitivity of the eROSITA sky survey is much lower than that of the targeted X-ray observations presented by Wang et al. (2021).

3.3. Spectrum

The integrated Stokes I spectrum of ASKAP J173608.2–321635 for the 2020 April 11 observation was found to have an in-band spectral index of $\alpha = -3.1 \pm 0.2$, where $S_\nu \sim \nu^\alpha$. This spectral index is within the range observed by Wang et al. (2021), which decreased from $\alpha = -2.7 \pm 0.1$ on 2021 February 7 to $\alpha = -5.6 \pm 0.3$ on 2021 April 25. We used our in-band spectral index to extrapolate L-band flux densities and upper limits to
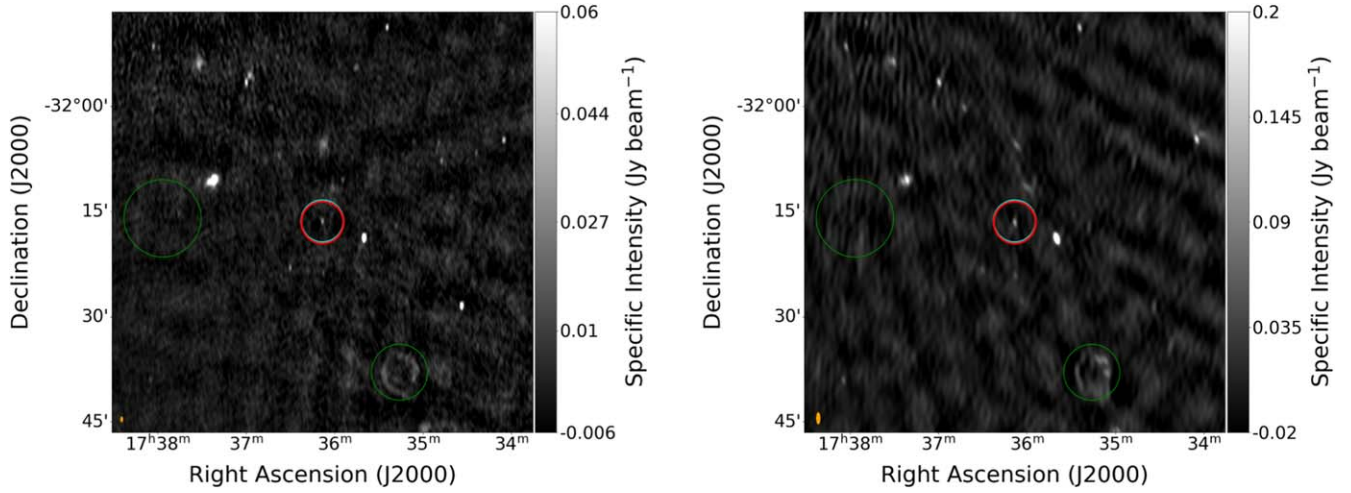
Figure 2. Images of ASKAP J173608.2–321635 and surroundings at 1029 MHz from THOR-GC (left) and at 339 MHz from VLITE (right). The red and blue circles are centered on the best-fit positions of ASKAP J173608.2–321635 from THOR-GC and VLITE, respectively. Green circles mark the locations and approximate angular size of supernova remnants in the catalog of Green (2019) updated in 2022.[16] Toward the left border is G356.3-0.3 (Gray 1994; Roy & Rao 2002), which is very diffuse and undetected in these narrow-band snapshots. Toward the bottom is G355.6-0.0 (Gray 1994; Roy & Bhatnagar 2006). The orange ellipses in the bottom left corners indicate the beam size in THOR (left) and VLITE (right).

900 MHz for direct comparison with the results of Wang et al. (2021; Figure 1). Our detection shows that ASKAP J 173608.2–321635 reached a peak brightness at least twice during its 2020/2021 period of activity, and its flux density dropped by a factor of ∼30 in between peaks.

The simultaneously measured VLITE flux density at 339 MHz is much lower than the extrapolated L-band spectrum would predict, as shown in Figure 3. This indicates a break in the radio spectrum that could be a feature of the mechanism that produces the radio emission. We will discuss synchrotron self-absorption in Section 5.2. This break implies that ASKAP J173608.2–321635 had an inverted low-frequency spectrum in contrast to the very steep spectrum of known GCRTs below ∼500 MHz (Hyman et al. 2007, 2009; Roy et al. 2010).

For our discussion it will be helpful to know what the opacity would be if the break were the result of free–free absorption. A power-law relation with free–free absorption ($S_\nu \sim \nu_{\mathrm{GHz}}^\alpha e^{-\tau\nu_{\mathrm{GHz}}^{-2}}$, where τ is the opacity at 1 GHz), with $\nu_{\mathrm{GHz}} = \nu/1\,\mathrm{GHz}$, fits the combined THOR-GC and VLITE data with $\alpha = -3.6 \pm 0.3$ and $\tau = 0.4 \pm 0.06$ at 1 GHz. Assuming a temperature of $10^4\,\mathrm{K}$, this free–free opacity corresponds to an emission measure of $\sim 1.1 \times 10^6\,\mathrm{cm}^{-6}\,\mathrm{pc}$. This is comparable to the emission measure of the Orion Nebula.

Rubin (1968) models the total flux density of optically thin free–free emission from regions of varying sizes as

$$S_\nu = \frac{8.61 \times 10^{-76}}{D^2 \nu^{0.1}} \int n_e n_i T^{-0.35} dV, \qquad (4)$$

where D is the distance in parsec, ν is the frequency in GHz, n_e and n_i are the electron and ion densities in cm^{-3}, dV is a volume element in cubic centimeters, and S_ν is in $\mathrm{ergs\,cm}^{-2}\,\mathrm{s}^{-1}\,\mathrm{Hz}^{-1}$. For an optically thin sphere with a 10 pc radius at a distance of 8.3 kpc (the distance to the Galactic center, GRAVITY Collaboration et al. 2021), assuming a uniform density of $2.0\,\mathrm{cm}^{-3}$, which is more normal for the inner Galaxy (Yao et al. 2017), and a temperature of $10^4\,\mathrm{K}$, we find 20 mJy for the flux density of free–free emission. This flux is high enough that it
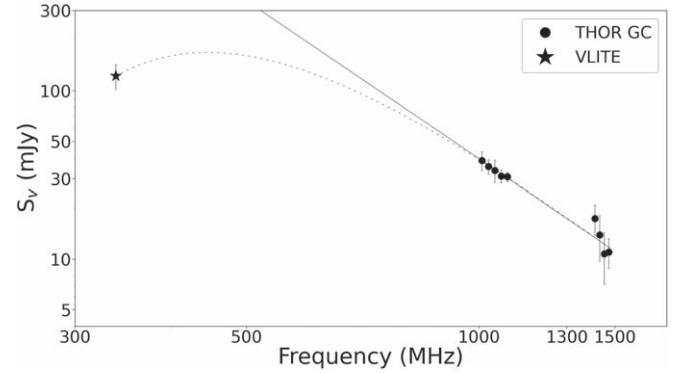

Figure 3. Stokes I flux density of ASKAP J173608.2–321635 from THOR-GC and VLITE observations on 2020 April 11. A power-law relation ($S_\nu \sim \nu^\alpha$) is fitted (solid) to the THOR-GC data with $\alpha = -3.1 \pm 0.2$. A power-law relation with free–free absorption is fitted (dashed) to the combined THOR-GC and VLITE data with $\alpha = -3.6 \pm 0.3$ and $\tau = 0.4 \pm 0.06$ at 1 GHz.

would have been detected in our measurements, but we do not see any persistent emission at the location of the source. If the radius of the sphere were 1 pc, the expected free–free emission would drop to $2 \times 10^{-2}\,\mathrm{mJy}$, which is below our detection threshold. As such, the observed spectral break could be due to a small region of plasma with a density predicted by the modeling, but only if its filling factor in the synthesized beam is very small. We will discuss the possibility that the spectral break is due to free–free absorption further in Section 5.

4. Polarization

The source was highly linearly polarized ($|L|/I \sim 76.7 \pm 3.9\%$, where $|L| = \sqrt{Q^2 + U^2}$) at 1.233 GHz, which is consistent with MeerKAT measurements of $|L|/I \sim 80\%$ (Wang et al. 2021). The RM of the source was determined using two methods: RM synthesis and QU fitting (Figure 4). RM synthesis found an RM of $+63.9 \pm 0.3\,\mathrm{rad\,m}^{-2}$. The RM value determined by QU fitting was consistent within the margin of error. QU fitting of Equation (3) also found the source to be depolarizing, with $\sigma_\phi = 4.8^{+0.5}_{-0.7}\,\mathrm{rad\,m}^{-2}$. Wang et al. (2021) found a similar
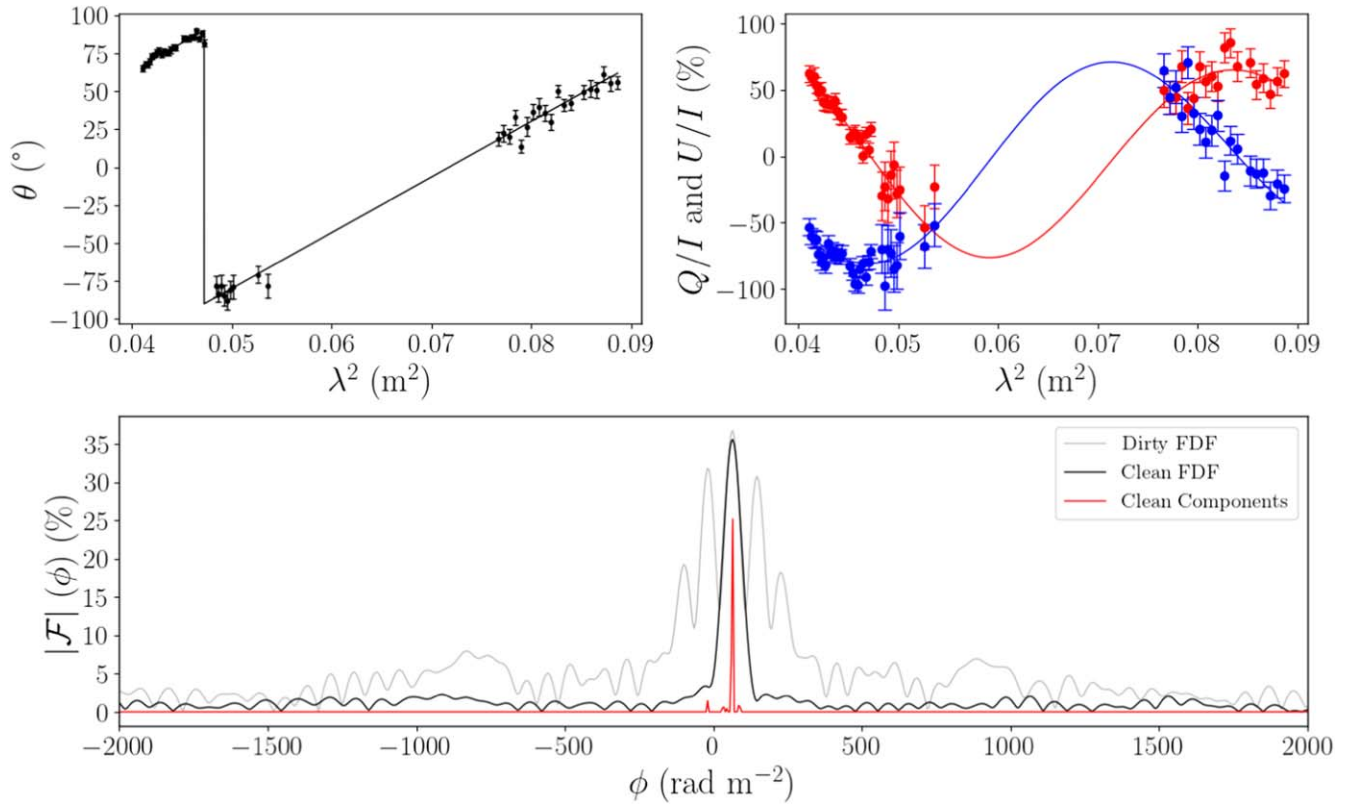
Figure 4. Results of QU fitting and RM clean for ASKAP J173608.2–321635 for the detection in THOR-GC on 2020 April 11. The top left panel shows the polarization angle as a function of λ^2 with the model from QU fitting. The top right panel shows Stokes Q (blue) and U (red) as a function of λ^2 with the result of QU fitting indicated by the solid lines. The bottom panel shows the dirty FDF in gray, the clean FDF and RM in black, and the clean components from RM clean in red.

depolarization, $\sigma_\phi = 5.7\,\mathrm{rad\,m^{-2}}$, on 2021 February 7, but found the RM to vary from $-11.8 \pm 0.8\,\mathrm{rad\,m^{-2}}$ on 2021 February 7 to $-64.0 \pm 1.5\,\mathrm{rad\,m^{-2}}$ on 2021 February 9. The THOR-GC measurement increases the RM variability range from ~ 50 to $\sim 130\,\mathrm{rad\,m^{-2}}$.

The polarization angle at the reference frequency 1.23 GHz is $-46°\!.7 \pm 0°\!.3$. Correcting for Faraday rotation, we find an intrinsic polarization angle of $97°\!.1 \pm 1°\!.9$ from RM synthesis and $96°\!.8^{+2.7}_{-3.1}$ from QU fitting. The uncertainty in the calibration of the absolute polarization angle is approximately $5°$ related to hour-angle and baseline-dependent effects in the RL phase that are not well understood (EVLA memo 205,[17] see also Lacy et al. 2020). The extrapolation to $\lambda = 0$ assumes a linear dependence between the polarization angle and λ^2 with slope RM at all wavelengths. We have no indication to the contrary, but the extrapolated polarization angle is only as good as this assumption (Farnsworth et al. 2011). Adding formal and absolute calibration errors in quadrature, we find an intrinsic polarization angle of $97° \pm 6°$.

The intrinsic polarization angle is related to the projection of the mean magnetic axis of the source on the plane of the sky. Wang et al. (2021) could not absolutely calibrate their polarization angles. They reported a reference source that could be used to calibrate the angle a posteriori. Unfortunately, this reference source is well below the detection limit of THOR-GC.

ASKAP J173608.2–321635 was not detected in circular polarization in our observation. We derive a 3σ upper limit of 2.0 mJy in Stokes V at 1248 MHz. As such, the fractional circular polarization of the source was less than 10.1% on 2020 April 11. This upper limit is well below some of the detections reported by Wang et al. (2021), before and after 2020 April 11 (Figure 1).

5. Discussion

5.1. RM Variability

Compared to the findings of Wang et al. (2021), the data presented in this paper reveal a much larger range of RM variability in ASKAP J173608.2–321635, notably changing the sign of RM. We also provide the first absolute polarization angle measurement, corrected for Faraday rotation, which may be important to establish whether the source has a stable magnetic axis in the plane of the sky.

The significance of the variable RM is best illustrated by a numeric example. RM is an integral quantity over the complete line of sight, but RM variability with an amplitude of order $10^2\,\mathrm{rad\,m^{-2}}$ is rare. Its origin must be sought in terms of a localized phenomenon associated with the source, as opposed to the ISM on larger scales, since the RM of most sources is not variable.

The distance traveled by relative motion with speed v in 1 yr is $d \approx 10^{-3} v_6\,\mathrm{pc}$, where v_6 has units of $1000\,\mathrm{km\,s^{-1}}$. The variation of RM is $\sim 10^2\,\mathrm{rad\,m^{-2}\,yr^{-1}}$ between 2020 April 11 and 2021 February 9, and $\sim 10^4\,\mathrm{rad\,m^{-2}\,yr^{-1}}$ between the two measurements by Wang et al. (2021) in 2021 February. If this change is effected by relative motion with a speed of order
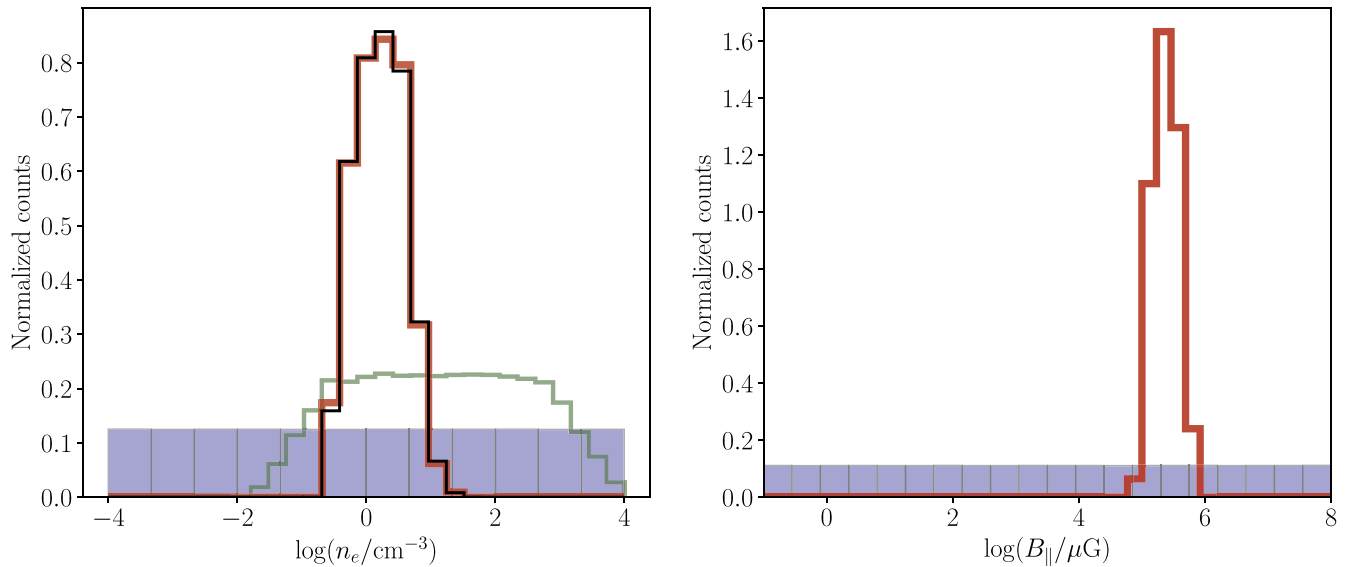
Figure 5. Distributions of n_e (left) and $B_{\parallel}$ (right) under the condition that $\nu_{\chi S}$ and ν_{rs} match the conditions described in the text. The blue histograms show the uniform distributions of the input parameters. The red histograms show the distributions that satisfy the conditions for both $\nu_{\chi S}$ and ν_{rs}. In the left panel, the green histogram shows the distribution that matches only the condition for $\nu_{\chi S}$ and the black histogram shows the distribution that matches only the condition for ν_{rs}. These distributions are not shown on the right, as they would both appear the same as the blue histogram.

$10^3 \, \mathrm{km \, s^{-1}}$, the line of sight scale of 10^{-3} pc indicates the variation of $n_e B_{\parallel}$ in the range of 10^5–$10^7 \, \mathrm{cm^{-3} \, \mu G}$. In the regular warm ionized medium, $n_e \sim 0.1 \, \mathrm{cm^{-3}}$, $B \sim 5 \, \mu G$, a distance 10^{-3} pc corresponds to an RM increment of order $2 \times 10^{-4} \, \mathrm{rad \, m^{-2}}$, which is 6 orders of magnitude smaller than the observed RM variability of ASKAP J173608.2–321635. Supernova remnants are believed to have $n_e B_{\parallel} \lesssim 10^3$ (Reynolds et al. 2012), and no supernova remnant is known to be associated with ASKAP J173608.2–321635 (Figure 2). The RM variability on timescales of days to several months suggests that the RM variability arises in an unusual plasma associated with the source.

5.2. Depolarization by Diffractive Scattering

Compared to the RM variability, the data indicate a very modest but non-zero Faraday depth dispersion. Our value is marginally smaller than that of Wang et al. (2021) at $\sigma_\phi \lesssim 5.7 \, \mathrm{rad \, m^{-2}}$. Faraday depth dispersion arises from differences in Faraday rotation between lines of sight that are combined within the beam. Instrumental Faraday depth dispersion arising from frequency averaging the visibilities to 4 MHz channels and fitting Equation (3) is less than $0.15 \, \mathrm{rad \, m^{-2}}$ for a source with RM = $63.9 \, \mathrm{rad \, m^{-2}}$. Equation (3) refers, strictly speaking, to a screen of turbulent cells with an angular size much smaller than the angular size of the background source. Considering the shortest known variability timescale of ASKAP J173608.2–321635, its angular size is of the order of a light day, or 21 mas at the distance of the Galactic center, 8.3 kpc. This is so small that we may suspect that the origin of the observed Faraday depth dispersion is different from the assumptions made in Equation (3).

Diffractive scattering is the distortion of the wave front by an intervening plasma, analogous to the effect of Earth's atmosphere on the light of a star causing seeing and scintillation (Williamson 1972; Rickett 1990). It gives rise to multiple signal paths through the ISM from the source to the observer. Several frequency-dependent effects are observable, such as pulse broadening for a pulsed source and scintillation,

which occurs for any source (pulsed or not) with an angular size smaller than the minimum angular size defined by the scattering plasma. These multiple signal paths also result in Faraday depth dispersion (see Equation (1)).

Galactic pulsars usually have negligible Faraday depth dispersion (Sobey et al. 2019). There are some exceptions, with pulsars displaying wavelength-dependent depolarization comparable to or more than what is measured for ASKAP J173608.2–321635(Sobey et al. 2021). Noutsos et al. (2009) found that the RM of some bright pulsars depends on the pulse phase with a range of order $10 \, \mathrm{rad \, m^{-2}}$, and attributed this to scattering. The effects of scattering of radio waves on the Faraday rotation of a source with very small angular size were recently described by Beniamini et al. (2022) in the context of FRBs. We analyze the Faraday depth dispersion of ASKAP J173608.2–321635 in the context of their model.

Beniamini et al. (2022) modeled diffractive scattering for FRBs, for which Feng et al. (2022) have presented a relation between pulse broadening and Faraday dispersion. The scattering in these sources occurs in a plasma close to the source, not in the Galactic ISM. Since ASKAP J173608.2–321635 is a compact source in a special environment, we can apply the model of Beniamini et al. (2022). A necessary but insufficient condition for depolarization is that the mean Faraday rotation angle $\Delta\theta \geqslant 1$ rad. Taking the RM variability amplitude as a lower limit of the mean RM of the plasma, this condition is satisfied for $\lambda^2 \gtrsim 6.7 \times 10^{-3} \, \mathrm{m^2}$, or $\nu \lesssim 3.7$ GHz. Wang et al. (2021) found depolarization for $\lambda^2 \gtrsim 0.05 \, \mathrm{m^2}$, roughly coincident with the emergence of detectable circular polarization at the $\gtrsim 10\%$ level. The total fractional polarization, including Stokes V, dropped significantly below 100%.

Beniamini et al. (2022) defined a critical frequency ν_{rs} for wavelength-dependent depolarization by a scattering screen, and frequency $\nu_{\chi S}$ below which circular polarization may arise from the scattering. Figure 5 shows the results of a parameter search that varied the electron density n_e, line-of-sight component of the mean magnetic field, $B_{\parallel}$, distance d, and

size of the scattering screen L. The distance was varied between 0.1 and 10 kpc, while the size of the scattering screen was varied between 10^{-4} pc and 1 kpc. The spectral resolution $\mathcal{R}$ was set to the THOR-GC resolution (4 MHz). All other model parameters were kept at the values assumed by Beniamini et al. (2022, see their Figure 3). We then constrained the models according to $1.1 < \nu_{\chi S} < 1.3$ GHz and $1.5 < \nu_{rs} < 2.5$ GHz. The distribution of allowed values for n_e and $B_\parallel$ are shown as red histograms in Figure 5. We find that both constraints are met if the density and magnetic field are within a factor of ~ 3 of $n_e = 2$ cm^{-3} and $B_\parallel = 2 \times 10^5$ μG. Interestingly, the strongest constraint on n_e comes from ν_{rs}, while both constraints are required to place limits on $B_\parallel$. The depth of the screen and the distance are not constrained by this experiment.

The model of Beniamini et al. (2022) thus implies a plasma with a density that is normal for the ISM in the Galactic center region (Yao et al. 2017) but a magnetic field that is several orders of magnitude stronger than typical ISM magnetic fields. We find $n_e B_\parallel \sim 10^5$–$10^6$ cm^{-3} μG, which is roughly consistent with the range estimated from the RM variability. The models approximately but not precisely reproduce the observed polarization of ASKAP J173608.2–321635. To give a specific example, assuming $n_e = 1.5$ cm^{-3}, $B_\parallel = 3.5 \times 10^5$ μG, $L = 10^{-3}$ pc, $d = 8.3$ kpc, velocity of the source 10^3 km s^{-1} and eddy velocity 100 km s^{-1} yield 1.39 GHz linear polarization 89%, circular polarization 4.5%, while at 1.0 GHz, the linear polarization is 76% and the circular polarization is 17%. These values approximate the observed fractional polarization and upper limits, but the frequencies $\nu_{\chi S} = 0.91$ GHz and $\nu_{rs} = 1.2$ GHz appear lower than the observations indicate.

The low-frequency spectral break reported here may be due to synchrotron self-absorption. Following Kellermann & Pauliny-Toth (1981) for the frequency of the peak brightness of a compact synchrotron source, with $B = 3 \times 10^5$ μG, peak flux density of 100 mJy, and angular size less than 21 mas, we find the peak brightness occurs at 220 MHz. With the same parameters, but the angular size of the source half the upper limit set by causality, the peak would occur near the VLITE frequency. So the parameters we find are consistent with the interpretation of the observed low-frequency spectral break in terms of synchrotron self-absorption. It should be kept in mind though, that the emission mechanism in ASKAP J173608.2–321635 may be more complex than the standard assumptions about synchrotron emission.

5.3. Nature of ASKAP J173608.2–321635 and the Scattering Screen

The upper range of magnetic field strength in supernova remnants is believed to be of order 1 mG (Reynolds et al. 2012) and the product $n_e B_\parallel \sim 10^3$ cm^{-3} μG is adopted for supernova remnants as environments for some FRBs (Yang et al. 2022b; Feng et al. 2022). The observed linear and circular polarization of ASKAP J173608.2–321635 requires a scattering screen with a magnetic field that is 2 orders of magnitude stronger, but one that is still weaker by many orders of magnitude than the magnetic field of a typical pulsar $\sim 10^{12}$ G (e.g., Philippov & Kramer 2022). Bearing in mind that the emission of ASKAP J173608.2–321635 may not be incoherent synchrotron emission, the synchrotron cooling time for electrons emitting GHz frequency synchrotron emission in a magnetic field of 10^6 μG is of the order of a month, which is too long to explain the observed variability on timescales of a day.

In the context of a compact source behind a scattering screen, a Faraday depth dispersion that is small compared with RM has been suggested as evidence of a large-scale magnetic field, or additional Faraday rotation in a separate plasma along the line of sight. However, when the RM is variable with a large amplitude over a short timescale, we must associate the RM itself with small-scale structure, and its variability with relative motions as outlined above. The implied plasma density $n_e \sim 2$ cm^{-3} is also too small to provide significant free–free opacity to explain the low-frequency spectral break reported in Section 3. The thermal emission of the scattering screen is undetectable because its filling factor in the synthesized beam is very small. In summary, we find that the scattering model by Beniamini et al. (2022) implies a plasma with unremarkable density but a strong magnetic field associated with ASKAP J173608.2–321635.

ASKAP J173608.2–321635 may be a high-velocity neutron star moving through the inner Galaxy. The physical scale for structure in the screen, $\sim 10^{-3}$ pc is not strongly constrained by the data, but it follows from the RM variability and a plausible but high speed. A highly supersonic neutron star, possibly with a pulsar wind, would create a bow shock structure. The distance between a highly supersonic pulsar and the apex of the contact discontinuity between a pulsar wind and the shocked ISM was given by Kargaltsev et al. (2017) as

$$R_a = 6.5 \times 10^{16} n^{-1/2} (f_\Omega \dot{E}_{36})^{1/2} v_7^{-1} \text{ cm}, \qquad (5)$$

and with $n = 2$ the particle density per cubic centimeter, $v_7 = 10$ the speed in 10^7 cm s^{-1}, $\dot{E}_{36} = 1$ the mechanical luminosity of the pulsar wind, and $f_\Omega = 1$, a dimensionless anisotropy factor, we find $R_a = 4.6 \times 10^{15}$ cm or $R_a = 1.5 \times 10^{-3}$ pc. The approximate scale of the screen and the relative speed of order 10^3 km s^{-1} match the shocked ISM in the bow shock of a high-velocity neutron star. The implied high magnetic field strength and modest density could arise in a turbulent wake.

The size of the radio emission region is less than a light day $(8.4 \times 10^{-4}$ pc) because of causality constraints and the rapid variability timescale reported by Wang et al. (2021). The emission of ASKAP J173608.2–321635 is more highly polarized than the theoretical maximum for optically thin incoherent synchrotron emission, which has fractional polarization $\lesssim 70\%$ to $\lesssim 85\%$ (higher if the power-law electron energy spectrum is steeper Pacholczyk 1977). Our data show that the source reached a maximum brightness in 2020 before dimming by a factor of ~ 30 and brightening again to the 2021 peak observed by Wang et al. (2021). This supports the idea of occasional brief enhanced injection (acceleration) of relativistic electrons into the emission region and that the variable, steep to ultra-steep, spectral index is related to the time of an observation since the injection of relativistic electrons.

The origin of the bursts requires speculation on the reason for the brief intermittent injection (acceleration) of relativistic electrons. The timescale between peak brightness appears to be months to years, suggested by a combination of modest sampling in time, detectable low-level emission in the period between the 2020 and 2021 peaks, and the fact that ASKAP J173608.2–321635 was not observed before 2020. Wang et al. (2021) did not detect pulsed emission but their observations were inconclusive because of the variability of the source. The absence of pulsation of (most of) the burst emission is significant because the physical scales derived from the variability allow an emission region that is orders of

magnitude larger than the radius of the light cylinder, $R_{LC} = 1.5 \times 10^{-9} P$ pc with P the pulsar's rotation period in seconds.

The variability of ASKAP J173608.2–321635 is unlike normal pulsars, so the mechanism of the bursts may be related to special conditions. It is interesting that the upper limit to the size of the emission region is comparable to the distance between the neutron star and the vertex point of the contact discontinuity between the pulsar wind and the swept-up medium. This leaves the possibility of injection of new particles into the magnetosphere because of a change in environment; for example, if ASKAP J173608.2–321635 runs into a structure in the ISM that changes the density or relative velocity of the surrounding medium. For a timescale of 1 yr between observed bursts, and a relative velocity of 10^3 km s^{-1}, the scale of a plasma structure would be of order 1.0×10^{-3} pc or ~200 au. Such plasma structures are known to exist from extreme scattering events (e.g., Coles et al. 2015). The physical scale is also similar to the size of the solar heliopause.

If ASKAP J173608.2–321635 is approximately at the distance of the Galactic center, it must be located well within the Fermi and eROSITA bubbles (Zhang & Guo 2020). The environment of ASKAP J173608.2–321635 may be very different from the ISM in the solar neighborhood, with a higher density of gas and stars, possibly stirred up by the activity of Sgr A* within the past $\lesssim$3 Myr (Guo & Mathews 2012; Yang et al. 2022a). This makes it plausible that the environment of ASKAP J173608.2–321635 changes on timescales shown in Figure 1 and is required by the RM variability when moving at its implied high speed.

The above picture of a highly supersonic pulsar running into a plasma structure, or perhaps the outskirts of another solar system, suggests it may be a rare kind of source with activity on a timescale of a year that may come to an end. Magnetohydrodynamic simulations of supersonic pulsars (Barkov et al. 2019; Bucciantini et al. 2020) model the interaction region as a steady, anisotropic pulsar wind that is generated at the light cylinder. Emission from the much larger interaction region between the pulsar wind and the ISM is not expected to be pulsed. We note that much older pulsars with a negligible pulsar wind may be better described by a magnetosphere interacting with the ISM, in analogy to a planetary magnetosphere that interacts with the solar wind.

Direct observations of the rapid evolution of the spectral index and possible time evolution of the spectral break reported here would provide valuable information on the emission mechanism and the particle acceleration process. This can be achieved by continued monitoring of this source and a more complete statistical sample of Galactic radio transients. The latter is a prospect for new radio telescopes with high survey speed, such as the Square Kilometre Array.

6. Summary and Conclusions

ASKAP J173608.2–321635 was detected with the VLA on 2020 April 11 with a flux density of 20.6 ± 1.1 mJy at 1.23 GHz and spectral index of $\alpha = -3.1 \pm 0.2$ (THOR-GC) and 339 MHz flux density of 122.6 ± 20.4 mJy (VLITE). The linear polarization at 1.23 GHz was $76.7 \pm 3.9\%$ and a 3σ upper limit for the circular polarization $|V|/I < 10.1\%$ was found.

On 2020 April 11 the RM of ASKAP J173608.2–321635 was 63.9 ± 0.3 rad m^{-2}. The RM of ASKAP J173608.2–321635 is

more variable than previously thought, and it changes sign. A basic geometric argument of the relative motion of a plasma and a compact source suggests that the Faraday rotation occurs in a plasma with $n_e B_\parallel$ of order 10^5–10^7 cm^{-3} μG, which is several orders of magnitude higher than the warm ionized ISM (WIM) and also 2 orders of magnitude beyond the range of $n_e B_\parallel$ thought to be representative for supernova remnants.

The simultaneous THOR-GC L-band and VLITE 339 MHz data reveal a low-frequency break in the spectrum of ASKAP J173608.2–321635. If this break is caused by free–free absorption, the free–free opacity at 1 GHz is $\tau = 0.4 \pm 0.06$. The thermal emission of such a plasma can only remain undetected if the filling factor within our beam is much smaller than 1. Such a plasma would almost certainly be associated with the source. However, free–free absorption is not consistent with our analysis of a scattering screen with a modest density of $n_e \sim 2$ cm^{-3}. The spectral break may be the result of synchrotron self-absorption in a source with an angular size of less than 21 mas, a magnetic field of ~3×10^5 μG, and a peak flux density of 100 mJy at a few hundred MHz.

The in-band depolarization of ASKAP J173608.2–321635 is quantified by Faraday depth dispersion $\sigma_\phi = 4.8^{+0.5}_{-0.7}$ rad m^{-2}, marginally smaller than the value reported by Wang et al. (2021). If this Faraday dispersion arises from scattering of radio waves in a plasma, the model by Beniamini et al. (2022) suggests the scattering plasma has a density that is comparable to WIM density near the Galactic center, but strongly magnetized with a magnetic field of the order of 3×10^5 μG.

We conclude that the variable RM and the Faraday depth dispersion of ASKAP J173608.2–321635 are consistent with the presence of a highly magnetized plasma associated with the source. This kind of plasma may be found in the wake of a high-velocity neutron star interacting with its environment.

ORCID iDs

Kierra J. Weatherhead ⓘ https://orcid.org/0009-0004-9607-721X
Jeroen M. Stil ⓘ https://orcid.org/0000-0003-2623-2064
Michael Rugel ⓘ https://orcid.org/0009-0009-0025-9286
Wendy M. Peters ⓘ https://orcid.org/0000-0002-5187-7107
Loren Anderson ⓘ https://orcid.org/0000-0001-8800-1793
Ashley Barnes ⓘ https://orcid.org/0000-0003-0410-4504
Henrik Beuther ⓘ https://orcid.org/0000-0002-1700-090X
Tracy E. Clarke ⓘ https://orcid.org/0000-0001-6812-7938
Sergio A. Dzib ⓘ https://orcid.org/0000-0001-6010-6200
Paul Goldsmith ⓘ https://orcid.org/0000-0002-6622-8396
Karl M. Menten ⓘ https://orcid.org/0000-0001-6459-0669
Kristina E. Nyland ⓘ https://orcid.org/0000-0003-1991-370X
Mattia C. Sormani ⓘ https://orcid.org/0000-0001-6113-6241
James Urquhart ⓘ https://orcid.org/0000-0002-1605-8050

References

Anderson, M. M., Mooley, K. P., Hallinan, G., et al. 2020, ApJ, 903, 116
Barkov, M. V., Lyutikov, M., & Khangulyan, D. 2019, MNRAS, 484, 4760
Beniamini, P., Kumar, P., & Narayan, R. 2022, MNRAS, 510, 4654
Beuther, H., Bihr, S., Rugel, M., et al. 2016, A&A, 595, A32
Brentjens, M. A., & de Bruyn, A. G. 2005, A&A, 441, 1217
Bucciantini, N., Olmi, B., & Del Zanna, L. 2020, JPhCS, 1623, 012002
Burn, B. J. 1966, MNRAS, 133, 67
CASA Team, Bean, B., & Bhatnagar, S. 2022, PASP, 134, 114501
CHIME Collaboration, Amiri, M., Bandura, K., et al. 2022, ApJS, 261, 29
Clarke, T. E., Kassim, N. E., Brisken, W., et al. 2016, Proc. SPIE, 9906, 99065B
Coles, W. A., Kerr, M., Shannon, R. M., et al. 2015, ApJ, 808, 113
Condon, J. J., Cotton, W. D., Greisen, E. W., et al. 1998, AJ, 115, 1693
Cotton, W. D. 2008, PASP, 120, 439
Croft, S., Bower, G. C., Ackermann, R., et al. 2010, ApJ, 719, 45
Farnsworth, D., Rudnick, L., & Brown, S. 2011, AJ, 141, 191
Feng, Y., Li, D., Yang, Y.-P., et al. 2022, Sci, 375, 1266

Frail, D. A., Kulkarni, S. R., Nicastro, L., Feroci, M., & Taylor, G. B. 1997, Natur, 389, 261
GRAVITY Collaboration, Abuter, R., Amorim, A., et al. 2021, A&A, 647, A59
Gray, A. D. 1994, MNRAS, 270, 847
Green, D. A. 2019, JApA, 40, 36
Greisen, E. W. 2003, in Astrophysics and Space Science Library, Vol. 285, Information Handling in Astronomy—Historical Vistas, ed. A. Heck, 285 (Berlin: Springer), 109
Guo, F., & Mathews, W. G. 2012, ApJ, 756, 181
Heald, G. 2009, in Cosmic Magnetic Fields: From Planets, to Stars and Galaxies, ed. K. G. Strassmeier, A. G. Kosovichev, & J. E. Beckman (Cambridge: Cambridge Univ. Press), 591
Hotan, A. W., Bunton, J. D., Chippendale, A. P., et al. 2021, PASA, 38, e009
Hyman, S. D., Roy, S., Pal, S., et al. 2007, ApJL, 660, L121
Hyman, S. D., Wijnands, R., Lazio, T. J. W., et al. 2009, ApJ, 696, 280
Jonas, J. & MeerKAT Team 2016, in Proc. of MeerKAT Science, of MeerKAT Science, 1
Kargaltsev, O., Pavlov, G. G., Klingler, N., & Rangelov, B. 2017, JPlPh, 83, 635830501
Kellermann, K. I., & Pauliny-Toth, I. I. K. 1981, ARA&A, 19, 373
Kramer, M., Lyne, A. G., O'Brien, J. T., Jordan, C. A., & Lorimer, D. R. 2006, Sci, 312, 549
Lacy, M., Baum, S. A., Chandler, C. J., et al. 2020, PASP, 132, 035001
Law, C. J., Gaensler, B. M., Bower, G. C., et al. 2011, ApJ, 728, 57
McLaughlin, M. A., Lyne, A. G., Lorimer, D. R., et al. 2006, Natur, 439, 817
Merloni, A., Lamer, G., Liu, T., et al. 2024, A&A, 682, A34
Murphy, T., Chatterjee, S., Kaplan, D. L., et al. 2013, PASA, 30, e006
Noutsos, A., Karastergiou, A., Kramer, M., Johnston, S., & Stappers, B. W. 2009, MNRAS, 396, 1559
O'Sullivan, S. P., Brown, S., Robishaw, T., et al. 2012, MNRAS, 421, 3300
Pacholczyk, A. G. 1977, OISNP, 89, 106
Petroff, E., Hessels, J. W. T., & Lorimer, D. R. 2022, A&ARv, 30, 2
Philippov, A., & Kramer, M. 2022, ARA&A, 60, 495
Polisensky, E., Lane, W. M., Hyman, S. D., et al. 2016, ApJ, 832, 60
Predehl, P., Andritschke, R., Arefiev, V., et al. 2021, A&A, 647, A1
Purcell, C. R., Van Eck, C. L., West, J., Sun, X. H., & Gaensler, B. M., 2020 RM-Tools: Rotation measure (RM) synthesis and Stokes QU-fitting, Astrophysics Source Code Library, ascl:2005.003
Reynolds, S. P., Gaensler, B. M., & Bocchino, F. 2012, SSRv, 166, 231
Rickett, B. J. 1990, ARA&A, 28, 561
Roy, S., & Bhatnagar, S. 2006, JPhCS, 54, 152
Roy, S., Hyman, S. D., Pal, S., et al 2010, ApJL, 712, L5
Roy, S., & Rao, A. P. 2002, MNRAS, 329, 775
Rubin, R. H. 1968, ApJ, 154, 391
Shanahan, R., Stil, J. M., Anderson, L., et al. 2022, ApJ, 939, 92
Schinzel, F.K. 2018, VLA polarization calibration: RL phase stability, Tech. Rep. EVLA Memo 205, https://library.nrao.edu/public/memos/evla/EVLAM_205.pdf
Sobey, C., Bilous, A. V., Grießmeier, J. M., et al. 2019, MNRAS, 484, 3646
Sobey, C., Johnston, S., Dai, S., et al. 2021, MNRAS, 504, 228
Stil, J. M., Taylor, A. R., Dickey, J. M., et al. 2006, AJ, 132, 1158
Tingay, S. J., Goeke, R., Bowman, J. D., et al. 2013, PASA, 30, e007
Tubín-Arenas, D., Krumpe, M., Lamer, G., et al. 2024, A&A, 682, A35
van Haarlem, M. P., Wise, M. W., Gunst, A. W., et al. 2013, A&A, 556, A2
Wang, Z., Kaplan, D. L., Murphy, T., et al. 2021, ApJ, 920, 45
Wang, Z., Murphy, T., Kaplan, D. L., et al. 2022, MNRAS, 516, 5972
Williamson, I. P. 1972, MNRAS, 157, 55
Yang, H. Y. K., Ruszkowski, M., & Zweibel, E. G. 2022a, NatAs, 6, 584
Yang, Y.-P., Lu, W., Feng, Y., Zhang, B., & Li, D. 2022b, ApJL, 928, L16
Yao, J. M., Manchester, R. N., & Wang, N. 2017, ApJ, 835, 29
Zhang, R., & Guo, F. 2020, ApJ, 894, 117